

# Multiband dispersion and warped vortices of strongly-interacting photons

Bankim Chandra Das, Dmytro Kiselov, Lee Drori, Ariel Nakav, Alexander Poddubny, and Ofer Firstenberg  
*Department of Physics of Complex Systems, Weizmann Institute of Science, Rehovot 7610001, Israel*

We study quantum correlations between interacting photons realized through co-propagating Rydberg polaritons. We show that the evolution of the  $n$ -photon wavefunction is governed by a multiband dispersion featuring one massive mode and  $n - 1$  degenerate modes, such as two Dirac cones for  $n = 3$ . The band structure exhibits an  $n$ -fold rotational symmetry, including an  $n$ -fold warped light cone, in contrast to the single-band, parabolic approximation often assumed for interacting polaritons. For three photons, the dispersion breaks the symmetry between a photon pair propagating ahead versus behind a single photon. We confirm these findings experimentally by measuring the three-photon phase and intensity correlation functions, revealing trigonal warping of the quantum vortex-ring generated by the three-photon interactions. Our analytical results are supported by rigorous numerical modeling that fully accounts for the photon propagation before, inside, and after the finite atomic medium. These findings advance the understanding of multi-photon interactions and the development of future multi-photon control tools.

Rydberg polaritons, formed by coupling propagating photons to Rydberg atoms in a dense atomic ensemble, provide a powerful platform for studying quantum interactions between a few particles [1, 2]. Their strong interactions arise from the long-range dipolar coupling between their Rydberg constituents. In the quantum nonlinear optics regime [3], Rydberg polaritons have been used to suppress the transmission of more than one propagating photons [4–7] and to demonstrate large conditional phase shifts [8, 9], bound states [10–12], and multimode interactions [13, 14] of two or three polaritons. Recently, stronger interactions enabled the observation of vortex-antivortex pairs in the two-polariton wavefunction  $\psi(x_1, x_2)$  and vortex rings and tubes in the three-polariton wavefunction  $\psi(x_1, x_2, x_3)$  [15]. Here,  $x_j$  are the photon coordinates along the propagation direction, *i.e.*, in one spatial dimension (Fig. 1a).

These developments establish Rydberg polaritons as a promising platform for multiphoton control and deterministic quantum logic. They also highlight the need for a rigorous theoretical framework to quantitatively describe quantum correlations arising from the propagation and interaction of several photons, including vortex formation. While previous theoretical models of interacting Rydberg polaritons — such as the adiabatic potential approximation [16], quantum field theory and Green function approaches [17–19], and waveguide quantum electrodynamics models [20–23] — offer valuable insights, they do not fully capture the spatial evolution of few-polariton wavefunctions in an extended medium. Although the model in Ref. [10] successfully describes two-polariton dynamics, it neither predicts the three-photon vortices observed in Ref. [15] nor captures their unique symmetry reported here. Moreover, its extension to higher-order correlations remains unclear.

Here, we develop a rigorous theoretical model describing  $n$ -photon interactions in finite extended media and experimentally validate its unique predictions for three photons. The model fully accounts for the multicom-

ponent structure of the wavefunction  $\psi(x_1, \dots, x_n)$ , revealing that  $\psi$  follows a multiband Dirac-like dispersion with one symmetric massive mode, separated by a finite gap from  $n - 1$  antisymmetric modes. For  $n \geq 3$ , the antisymmetric modes are point-degenerate at zero momentum and exhibit linear dispersion. As an approximation, these antisymmetric modes can be eliminated by assuming they adiabatically follow the massive mode, thereby reducing the model to a Schrödinger-like equation for a single (massive) mode in  $n - 1$  dimensions with an  $(n!)$ -fold symmetry. This approximation, previously used in two- and three-photon systems, has provided valuable insight into the polariton dynamics in terms of bound states [10, 12]. However, as shown in Fig. 2, the parabolic single-band approximation fails to retain key features of the multiband structure, particularly the linear-dispersion regions and the reduced  $n$ -fold discrete rotational symmetry. Both are essential for describing the evolution in finite media and capturing the effects of interaction-dependent group velocity.

The multiband dispersion significantly impacts photon correlations starting from  $n = 3$  photons. It reduces the wavefunction’s rotational symmetry (from  $3! = 6$  to 3) by distinguishing between cases where a photon pair propagates ahead of or behind a single photon. This symmetry reduction was previously detected at a few-percent level in photon correlation functions with a single atom or effective superatom (a fully-blockaded Rydberg ensemble) [11, 24, 25]. Here, we observe it experimentally at near-unity levels, manifesting as a trigonal warping of the vortex ring formed by three-photon interactions. The presented data result from a new analysis of experiments reported in Ref. [15], which does not assume a 6-fold rotational symmetry. We provide analytical and numerical models capturing the dynamics inside and outside the finite atomic medium and reproducing the experimental results.

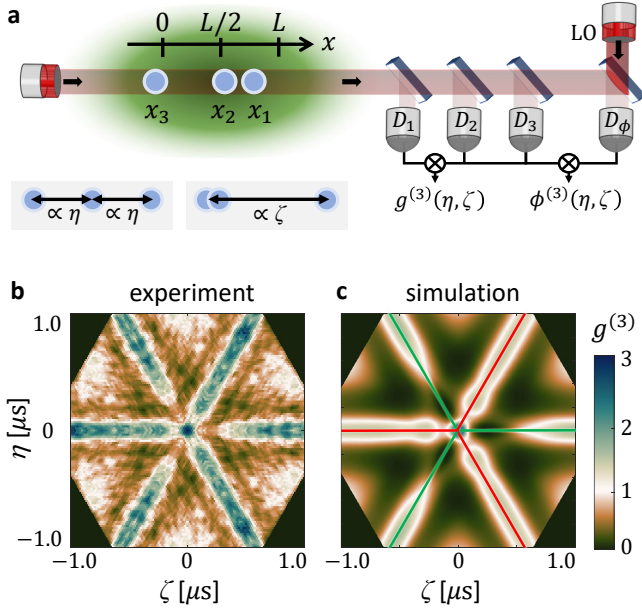


FIG. 1. **System of interacting photons and correlation measurements.** (a) Photons at coordinates  $x_i$  travel along the atomic medium. The three-photon correlation function  $g^{(3)}$  is measured using detectors  $D_{1,2,3}$ , while the conditional phase  $\phi^{(3)}$  is obtained by mixing outgoing photons with a local oscillator (LO) and correlating the beat note at  $D_\phi$  with photon pairs in  $D_{1,2,3}$ . Temporal Jacobi coordinates  $\eta$  and  $\zeta$  (gray panels) represent the time separations between outgoing photons. (b) Experimentally observed  $g^{(3)}(\eta, \zeta)$  and (c) corresponding numerical simulation, revealing strong asymmetry between a photon pair propagating behind or ahead of a single photon, marked by green and red lines, respectively (same color code throughout). See Methods for experimental and simulation parameters.

### Multiband model for two and three photons

We begin with a minimal theoretical model that correctly captures the symmetry of few-polariton states. Consider a medium of three-level ladder-type atoms hosting Rydberg polaritons in the regime of electromagnetically induced transparency [4, 26]. The stationary single-polariton propagation along the medium is governed by  $H(x)\psi = 0$ , where

$$H(x) = - \begin{pmatrix} ic\partial_x & \sqrt{\rho}g & 0 \\ \sqrt{\rho}g & \Delta + i\Gamma & \Omega \\ 0 & \Omega & \delta + i\gamma \end{pmatrix} \quad (1)$$

is the effective Hamiltonian for the atoms and photon. The polariton wavefunction  $\psi(x) = [E(x), P(x), S(x)]^T$  consists of amplitudes  $E(x)$  for a single photon (all atoms in the ground state  $|g\rangle$ ),  $P(x)$  for one atom in the intermediate state  $|p\rangle$ , and  $S(x)$  for one atom in the Rydberg state  $|s\rangle$ . Here,  $g$  is the coupling strength of the photon to the  $|g\rangle \leftrightarrow |p\rangle$  transition,  $\rho$  is the medium density,  $\Omega$  is the Rabi frequency of the  $|p\rangle \leftrightarrow |s\rangle$  driving,  $\Gamma$  is the decay rate of  $|p\rangle$ ,  $\gamma$  is the decoherence rate of  $|s\rangle$ , and  $\Delta$  and  $\delta$

are the one-photon and two-photon detunings. We consider  $|\Delta| \gg \Gamma$  and, for simplicity, assume  $\Gamma = \delta = \gamma = 0$ . Since  $|p\rangle$  and  $|s\rangle$  are dispersionless in Eq. (1), they can be eliminated from  $H(x)\psi = 0$ , reducing the system to the single-component equation:

$$[ic\partial_x - \omega_D]\psi_1(x) = 0 \quad \text{for } \psi_1(x) \equiv E(x). \quad (2)$$

Here,  $ic\partial_x$  arises from the bare photon dispersion, and the shift  $\omega_D = \rho g^2 / \Delta$  stems from the photon hybridization with the atomic states.

Equation (2) straightforwardly generalizes to two and three interacting polaritons, characterized by the multicomponent wavefunctions  $\psi$ . In the minimal model, where the atomic states are eliminated, each component in  $\psi$  corresponds to a single propagating photon with the other excitations residing in the Rydberg states:  $\psi = [ES, SE]$  for two polaritons and  $\psi = [ESS, SES, SSE]$  for three. The result is

$$\begin{aligned} ic \begin{pmatrix} \partial_{x_1} & 0 \\ 0 & \partial_{x_2} \end{pmatrix} \psi - \tilde{\omega}_D \psi + \frac{V_2}{2} \begin{pmatrix} 1 & 1 \\ 1 & 1 \end{pmatrix} \psi &= 0, \\ ic \begin{pmatrix} \partial_{x_1} & 0 & 0 \\ 0 & \partial_{x_2} & 0 \\ 0 & 0 & \partial_{x_3} \end{pmatrix} \psi - \tilde{\omega}_D \psi + \frac{V_3}{3} \begin{pmatrix} 1 & 1 & 1 \\ 1 & 1 & 1 \\ 1 & 1 & 1 \end{pmatrix} \psi &= 0, \end{aligned} \quad (3)$$

where  $\tilde{\omega}_D = \omega_D + \Omega^2 / \Delta$ .

A key feature of Eqs. (3) is the all-to-all interaction between the wavefunction components, arising from their coupling to the state with all excitations in the Rydberg state ( $SS$  or  $SSS$ ). The interaction potentials  $V_2$  and  $V_3$  originate from van-der-Waals (vdW) interactions between the Rydberg atoms and depend on the polariton coordinates,

$$V_n = \omega_D \left( 1 + \frac{2}{n} \sum_{i,j=1; i \neq j}^n \frac{r_b^6}{|x_i - x_j|^6} \right)^{-1} \quad (4)$$

for  $n \geq 2$  polaritons, where  $C_6$  is the vdW coefficient. The potentials vanish inside the ‘Rydberg blockade’ volume, when any two polaritons are closer than the blockade radius  $r_b = (C_6 \Delta / 2\Omega^2)^{1/6}$ , and approach the constant value  $\omega_D$  at large separations. In a homogeneous medium, Eqs. (3) remain independent of the normalized center-of-mass coordinate  $R = \sum_{i=1}^n x_i / \sqrt{n}$ . Thus, it is useful to introduce the normalized relative coordinates:  $r = (x_1 - x_2) / \sqrt{2}$  for  $n = 2$  and the spatial Jacobi coordinates  $\eta = x_{12} / \sqrt{2}$  and  $\zeta = (x_{13} + x_{23}) / \sqrt{6}$  for  $n = 3$ , with  $x_{ij} = x_i - x_j$ .

Before discussing interaction effects between polaritons, we examine the dispersion in Eqs. (3) outside the blockade region. To this end, we assume translational invariance and replace the spatial derivatives  $-i\partial_R$ ,  $-i\partial_r$ , and  $-i\partial_{\eta, \zeta}$  by the corresponding momenta  $K$ ,  $k$ , and  $k_{\eta, \zeta}$ . This allows Eqs. (3) to be solved for the normalized center-of-mass momentum  $K$  as a function of  $k$  and

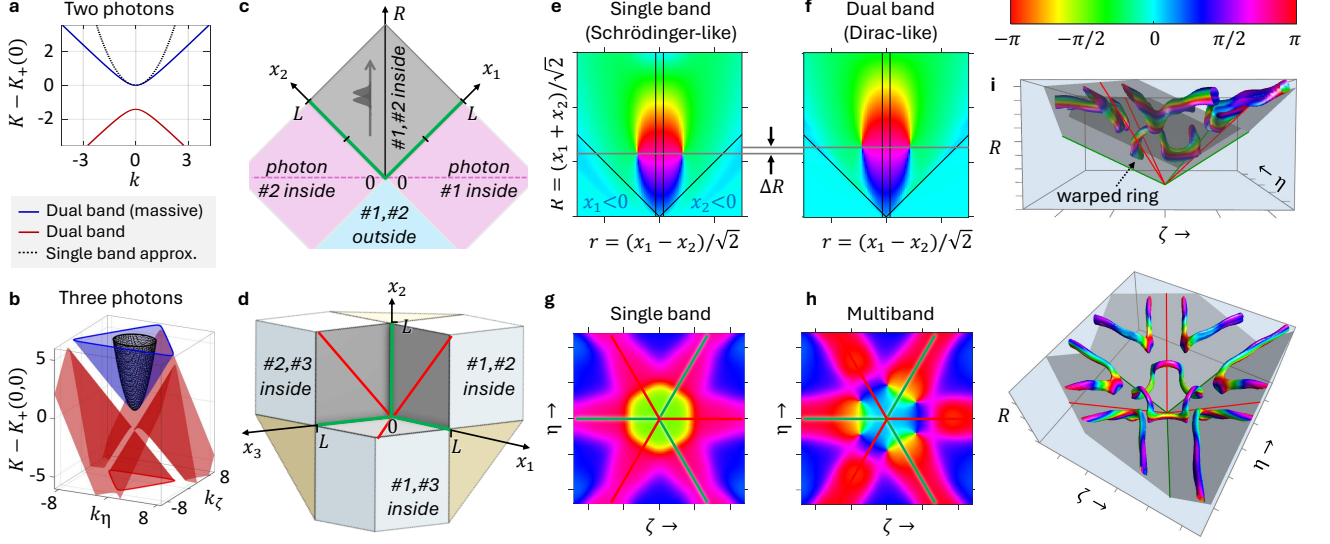


FIG. 2. **Analytical multiband model – Momentum-space dispersion and real-space propagation of two and three photons.** (a) **Two-photon dispersion:** Center-of-mass dispersion  $K(k)$  for two non-interacting polaritons. The dashed line represents the single-band Schrödinger approximation of the massive polariton branch, while the solid lines show the full two-band Dirac-like dispersion. (b) **Three-photon dispersion:** Center-of-mass dispersion  $K(k_\eta, k_\zeta)$  for three polaritons, highlighting the emergence of trigonal warping. The black surface represents the single-band Schrödinger approximation, which fails to capture the warping.  $K(k)$  and  $K(k_\eta, k_\zeta)$  are solved via Eqs. (3), the offsets are  $K_+(0)/\sqrt{2} = K_+(0,0)/\sqrt{3} = \Omega^2/(c\Delta)$ , and all units in  $\rho g^2/(c\Delta)$ . (c) **Two-photon coordinate space:** Schematic showing the propagation center-of-mass coordinate  $R$  and relative coordinate  $r$ . Two-photon interaction occurs only inside the medium ( $0 < x_{1,2} < L$ , gray area). The entry points  $x_1 = 0$  and  $x_2 = 0$  (green lines) serve as light-cone boundaries, below which two-photon correlations cannot develop. (d) **Three-photon coordinate space:** Interaction occurs already when photon pairs are inside the medium (light blue sections), while full three-photon interaction requires all  $0 < x_{1,2,3} < L$ . Regions above the green (red) lines correspond to a closely spaced photon pair propagating behind (ahead of) a single photon. (e,f) **Two-photon phase profiles:** The phase of the two-photon wavefunction under the single-band model (e) shows a vortex-antivortex pair at finite propagation distance  $R$  (gray line) but also unphysical correlations outside the light-cone boundaries ( $x_{1,2} < 0$ ). The full two-band dispersion (f) corrects the unphysical behavior, confining correlations within the light cone and introducing a propagation delay  $\Delta R$  in vortex formation. (g-i) **Three-photon phase profiles:** The phase of the three-photon wavefunction under the single-band model (g) retains a 6-fold rotational symmetry and fails to capture the warping. The multiband model (h) reduces the rotational symmetry to 3-fold, with the delay  $\Delta R$  observed for two photons manifesting here as a delay of the vortex formation along the pair-ahead (red) lines. In (i), the isosurfaces of  $|\nabla \arg(\psi)|$  reveal a vortex ring with trigonal warping, a hallmark of the three-photon interaction captured by the multiband model. Calculations in (f,h,i) follow Eqs. (29)–(32) in Methods.

$\vec{k} = (k_\eta, k_\zeta)$ . The resulting  $K(k)$  and  $K(\vec{k})$  for two and three photons, respectively, are shown in Figs. 2a and 2b [see Eqs. (14) and (19,20) in Methods]. For two photons, we obtain the characteristic Dirac dispersion. At  $k = 0$ , there is a gap, and the eigenstates are the even and odd superpositions,  $ES_\pm = (ES \pm SE)/\sqrt{2}$ . Near  $k = 0$ , the dispersion is parabolic (dotted curve in Fig. 2a), corresponding to the Schrödinger approximation [4, 10],

$$i \frac{\partial}{\partial R} ES_+ = \left( -\frac{1}{2m} \frac{\partial^2}{\partial r^2} + \frac{\sqrt{2}\omega_D}{c} - \frac{\sqrt{2}V_2}{c} \right) ES_+, \quad (5)$$

where  $m = -\omega_D/(\sqrt{2}c)$  is the effective mass. However, for large  $k$ , the dispersion becomes linear and deviates from the Schrödinger approximation.

The difference between the parabolic approximation and the full model is more pronounced for three photari-

tons, as shown in Fig. 2b. At  $\vec{k} = 0$ , solving Eq. (3) for  $K$  yields one symmetric state,  $ESS_+ = (ESS + SES + SSE)/\sqrt{3}$ , and two degenerate antisymmetric states,  $ESS_- = (ESS - SES)/\sqrt{2}$  and  $ESS'_- = (ESS + SES - 2SSE)/\sqrt{6}$ . For  $\vec{k} \neq 0$ , the symmetric state  $ESS_+$  acquires mass, while the two antisymmetric states split, forming characteristic Dirac cones (red in Fig. 2b). Far from  $\vec{k} = 0$ , all three states mix, yielding warped dispersion with  $C_{3v}$  symmetry. This effect is similar to the trigonal warping of Dirac cones in graphene [27], where warping arises from the crystalline symmetry. Here, it emerges naturally from the three-polariton coupling and permutation symmetry. Importantly, this warping cannot be captured by the parabolic Schrödinger equation [28], which approximates the warped cone as a rotationally symmetric paraboloid (Fig. 2b).

## Real-space consequences

We now demonstrate how the difference between the single-band Schrödinger and multiband Dirac-like dispersions manifests in the real-space wavefunctions. For simplicity, we consider a uniform medium of length  $L$  (one typically chooses  $L \approx \sqrt{2\pi}\sigma$  for a Gaussian cloud with width  $2\sigma$  [15]). For two photons, it is instructive to divide the Hilbert space into quadrants corresponding to zero, one, or two photons inside the atomic medium, as shown in Fig. 2c. Photon-photon interaction, mediated by the atoms, occurs only when both photons are inside (*i.e.*, in the gray-shaded quadrant  $0 < x_{1,2} < L$ ). The green lines  $x_1 = 0$  and  $x_2 = 0$ , marking the entry points of the first and second photons, define the boundary conditions for the onset of interaction. These lines serve as effective light-cone boundaries for the development of correlations. Nevertheless, to simplify semi-analytic modeling, the boundary conditions are typically adjusted so that the interaction begins earlier, at  $R = 0$  for all  $r$  (dashed line in Fig. 2c) [10, 15]. Initially uncorrelated photons are represented by the wavefunction  $\psi(R = 0, r) = 1$ , which accumulates phase as it propagates.

The steady-state wavefunction in the single-band Schrödinger approximation is shown in Fig. 2e. Phase accumulates more rapidly when photons are close together, generating vortex-antivortex pairs. The generation mechanism is robust, as it results from interference between the two-photon bound state and the unbound part of the wavefunction [15]. While the single-band model predicts these vortices, it also produces unphysical correlations below the light-cone boundaries  $R = |r|$  (*i.e.* at  $x_{1,2} < 0$ , where only one photon is inside). These arise because the Schrödinger equation does not impose a speed limit on information propagation.

By contrast, the dual-band Dirac-like model, Eq. (3), naturally enforces the light-cone limits, as seen in Fig. 2f. Furthermore, since two-photon interaction starts only at  $R = |r|$  in the dual-band model, the vortices shift forward by  $\Delta R$ . This shift can thus be understood as a consequence of the light-cones limits imposed on the phase pattern in Fig. 2f.

For three photons, the impact of the multiband dispersion is more pronounced and includes symmetry reduction. We first analyze this effect analytically. The space  $(x_1, x_2, x_3)$  is divided into sections based on the number of photons inside the medium (Fig. 2d). The faces of the three-photon section  $0 < x_{1,2,3} < L$  (gray shaded) act as effective light-cone boundaries, warping the wavefunction. To understand the warping symmetry, we identify two types of regions in that section: Three ‘single ahead’ regions, where a single photon propagates ahead of a tight photon pair (*e.g.*,  $x_1 \approx x_2 < x_3$ , or  $\zeta < 0$  for  $\eta \approx 0$ ), and three ‘pair ahead’ regions, where a single photon lags behind a pair (*e.g.*,  $x_3 < x_1 \approx x_2$ , or  $\zeta > 0$  for  $\eta \approx 0$ ). The single-ahead regions of the wavefunction

evolve predominantly from the section edges (green lines in Fig. 2d,g-i), while the pair-ahead regions evolve from the face centers (red lines).

As evident from the geometry, single-ahead configurations begin to experience three-photon interaction at an ‘earlier’  $R = (x_1 + x_2 + x_3)/\sqrt{3}$  compared to pair-ahead configurations. They develop stronger correlations during propagation, further reducing the wavefunction symmetry. This effect is amplified by the group velocity dependence on photon-photon interaction. Since a closely spaced photon pair moves faster than a single photon [10, 23, 28], the single-ahead configurations gradually compact and interact more, while in pair-ahead configurations, the single photon lags behind. This behavior is captured by the multiband model Eq. (3) in numerical wavefunction evolution (Fig. 2h). It yields a reduced  $C_{3v}$  symmetry, with correlations building up faster for single-ahead compared to pair-ahead configurations. In contrast, the single-band model retains the  $C_{6v}$  symmetry (Fig. 2g). The three-photon interaction ultimately produces a phase vortex ring [15], which the multiband model predicts to exhibit a trigonal warping (Fig. 2i). We further explore this warping in the next section.

Figure 1b provides experimental evidence of the broken  $C_{6v}$  symmetry in  $g^{(3)}(\eta, \zeta)$  measurements. Here  $\eta = t_{21}/\sqrt{2}$  and  $\zeta = (t_{13} + t_{23})/\sqrt{6}$  are the temporal Jacobi coordinates ( $t_{ij} = t_i - t_j$ ). Note that the  $\zeta$  values for pair-ahead and single-ahead configurations have opposite signs compared to the spatial  $\zeta$ . In the data, the pair-ahead configuration (red lines) exhibits bunching ( $g^{(3)} > 1$ ), due to two-photon attraction [10] and remains largely unaffected by the lagging photon. Conversely, in the single-ahead configuration (green lines) the pair attracts the leading photon, reducing the probability of detecting the triplet ( $g^{(3)} < 1$ ) at a finite time interval.

To analyze these results and the vortex warping, we developed a full numerical model to simulate the exact dynamics in a Gaussian-shaped atomic cloud, extending previous two-photon models [4, 26]. The model, detailed in Methods, covers all 27 space sections. It provides the complete three-photon wavefunction  $\psi(x_1, x_2, x_3)$  with its  $3^3 = 27$  components inside the cloud (central section), as well as the experimentally accessible correlation functions  $g^{(3)}$  and  $\phi^{(3)}$  as a function of the photon detection times outside of the cloud. The latter involves propagating the remaining two (or one) photons, conditioned on the detection times of the first (or second) photon. Figure 1c presents the simulated  $g^{(3)}$ , accurately capturing all experimental features.

### Trigonal warping of three-photon vortices

We use simulations to explore the three-photon vortex formation, as shown in Fig. 3. For reference, Fig. 3a presents the vortex-antivortex pair in the two-photon wavefunction. A vortex is always accompanied by an antivortex due to the bosonic symmetry,

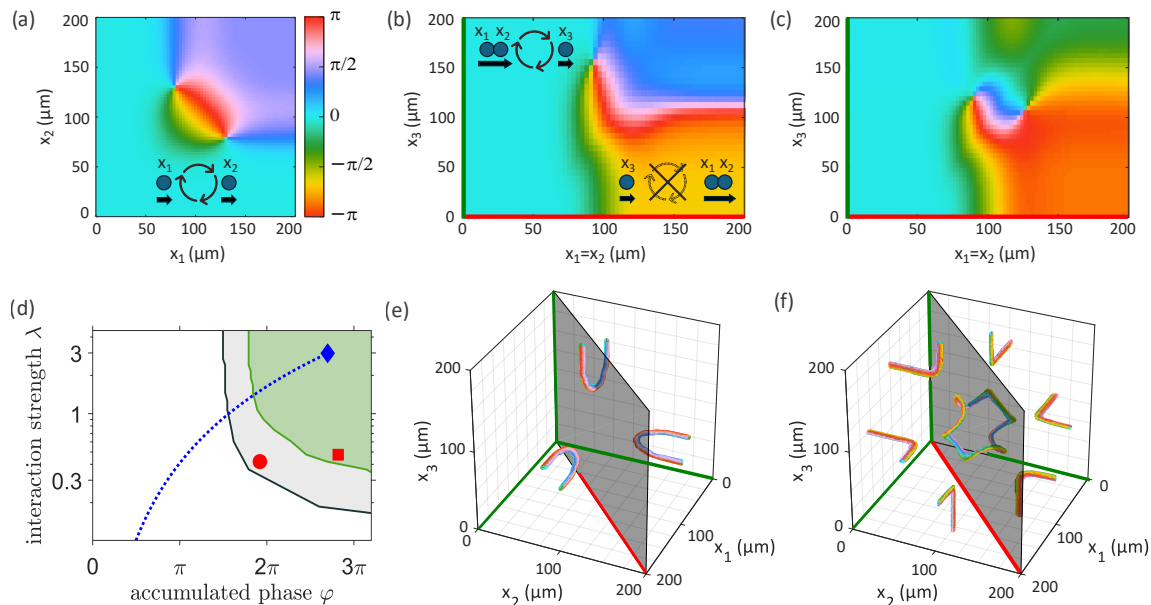


FIG. 3. **Numerical simulations of three-photon vortices with three-fold rotational symmetry  $C_{3v}$ .** The Gaussian-shaped atomic cloud ( $\sigma = 30 \mu\text{m}$ ) with OD = 78 – 115 is centered at  $x = 100 \mu\text{m}$ . **(a)** Phase of the stationary two-photon wavefunction  $\psi(x_1, x_2)$ , showing a symmetric vortex-antivortex pair. **(b,c,e,f)** Phase of the stationary three-photon wavefunction  $\psi(x_1, x_2, x_3)$ , displaying different vortex tube and ring configurations for (b,e) intermediate and (c,f) strong interactions. (e,f) show isosurfaces of  $|\nabla \arg(\psi)|$ , while (b,c) present cross-sections of  $\arg(\psi)$  along the shaded planes in (e,f). For an intermediate interaction strength (b,e), three-photon vortex tubes form only in the single-ahead configurations (e.g.,  $x_1 \approx x_2 < x_3$ ), consistent with faster pair propagation. For longer and stronger interactions (c,f), vortex tubes also form in the pair-ahead configurations (e.g.,  $x_3 < x_1 \approx x_2$ ), and the six tubes merge into a warped vortex ring with a reduced  $C_{3v}$  symmetry. **(d) Phase diagram of three-photon vortex formation.** The shaded regions mark the parameter regimes for (gray) single-ahead and (green) pair-ahead vortices as a function of interaction strength ( $\lambda$ ) and duration ( $\varphi$ ). The blue diamond and dotted line represent the experimental conditions, while the red circle and square correspond to the conditions of (b,e) and (c,f), respectively. See Methods for definitions and model parameters.

$\psi(x_1, x_2) = \psi(x_2, x_1)$ . For the three-photon wavefunction  $\psi(x_1, x_2, x_3)$ , while the  $C_{3v}$  bosonic symmetry naturally holds, the single-ahead ( $x_1 \approx x_2 < x_3$ ) and pair-ahead ( $x_3 < x_1 \approx x_2$ ) configurations differ significantly.

At intermediate interaction strengths (Fig. 3b), vortices form only in the single-ahead configuration. Increasing the interaction enables vortices in both configurations (Fig. 3c), though the wavefunction remains asymmetric. The phase diagram in Fig. 3d maps the parameter regimes for forming single-ahead vortices (gray shading) and all vortices (green shading). We quantify the interaction strength and duration using the dimensionless parameters  $\lambda \propto \text{OD}_b^2$  and  $\varphi \propto \text{OD}$ , respectively [15] (see Methods for exact expressions). Here, OD is the optical depth of the medium, and  $\text{OD}_b = \text{OD} \cdot r_b / L$  is the optical depth of the blockade range. Similar to the threshold for two-photon vortices [15], we identify thresholds for both types of three-photon vortices (black and green lines).

Figures 3(e,f) illustrate the corresponding three-dimensional vortex structures. The first regime is characterized by three disconnected vortex tubes, each originating from a single-ahead vortex. In the second regime, three additional vortex tubes emerge from pair-ahead vortices before the third photon enters. The tubes gen-

erally merge into a central vortex ring, either inside the medium or during outward propagation. The vortex topology in the first regime and ring's warping in the second regime clearly reflect the trigonal symmetry of the underlying dispersion and the light-cone boundaries.

We now turn to the experimental verification of these predictions. Since direct access to the wavefunction inside the medium is not possible, we reconstruct its topology by probing the conditional phase of photons existing the medium,  $\phi^{(3)}$ , for a range of ODs [15]. The experimental conditions realized in our setup are shown in Fig. 3d (blue). Figures 4(a-f) present a revised analysis of the data from Ref. [15], now assuming only  $C_{3v}$  symmetry instead of  $C_{6v}$ . A clear asymmetry  $\phi^{(3)}(\eta, \zeta, \text{OD}) \neq \phi^{(3)}(\eta, -\zeta, \text{OD})$  is observed in the planar cross-sections and three-dimensional views. The vortex ring in  $\phi^{(3)}(\eta, \zeta, \text{OD})$  exhibits strong warping, as predicted, similar to the stationary vortex ring in  $\psi(x_1, x_2, x_3)$  inside the cloud. The corresponding simulation, incorporating the temporal evolution of the wavefunction after the first and second photon detections, is shown in Fig. 4. It reproduces the  $C_{3v}$  symmetry and the warping of the vortices.

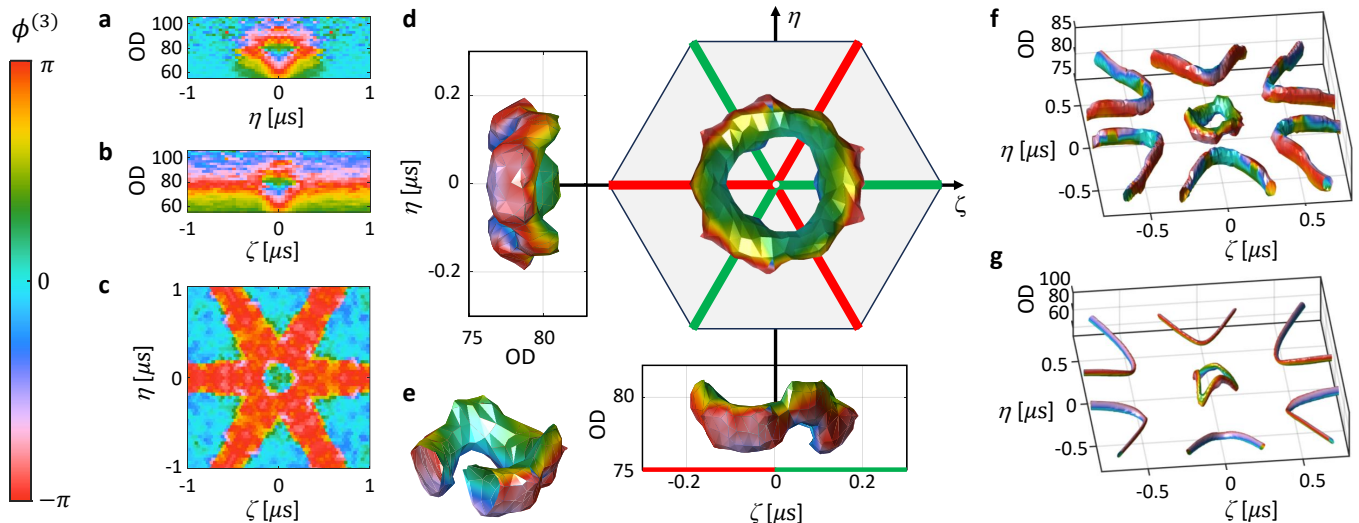


FIG. 4. **Experimental observation of three-photon vortex ring with trigonal warping.** **a-c**, Measured conditional phase  $\phi^{(3)}(\eta, \zeta, \text{OD})$  as a function of optical depth (OD). We show cross-sections through the center of the vortex ring at (a)  $\zeta = 0$ , (b)  $\eta = 0$ , and (c)  $\text{OD}=79$ . Single-ahead vortices ( $\zeta > 0$  along  $\eta = 0$ ) form at lower OD than pair-ahead vortices ( $\zeta < 0$ ), leading to a  $C_{3v}$  symmetry in (c). **d-f**, Different viewing angles and a sectional view of the vortex structure, obtained by plotting  $\phi^{(3)}$  on isosurfaces of  $|\nabla\phi^{(3)}|$ , clearly revealing a vortex ring with trigonal warping. **g**, Corresponding simulation of three-photon propagation and subsequent detection, reproducing the tube and ring structures with  $C_{3v}$  symmetry and warping.

### $n$ -photon model and outlook

The multiband model Eqs. (3) extends naturally to  $n > 3$  photons, yielding the system of  $n$  equations

$$i\frac{\partial\psi_i}{\partial t} = -ic\frac{\partial\psi_i}{\partial x_i} + \tilde{\omega}_D\psi_i + \frac{1}{n}V_n(x_1, \dots, x_n)\sum_{i=1}^n\psi_i \quad (6)$$

(see Methods), where  $\psi_i$  is the wavefunction amplitude with the  $i$ -th polariton in state  $E$  and the others in state  $S$ , and  $V_n$  is the rescaled vdW interaction potential Eq. (4). In the blockade range, where any two polaritons are close,  $V_n = 0$ . Without the interaction term  $V_n \sum_{i=1}^n \psi_i$ , Eq. (1) describes  $n$  free photons, each propagating independently with linear (massless) dispersion,  $\psi_i \propto e^{-i\omega_{k_i}t + ik_i x_i}$ , where  $\omega_k = ck$ ,  $k_i$  is the wave vector of  $i$ -th photon, and we assume the translation invariance. Since the photons are hybridized with the Rydberg state, the coupling term persists even at large separations, where  $V_n$  approaches the constant  $V_{n,\infty} = \omega_D$ .

Following the approach for  $n = 2, 3$ , we solve Eq. (6) in a translationally invariant system for the normalized center-of-mass momentum  $K = \sum_{i=1}^n k_i / \sqrt{n}$ . We identify one massive mode with all  $\psi_i = 1/\sqrt{n}$  and  $n - 1$  degenerate modes with  $\sum_{i=1}^n \psi_i = 0$ . The massive mode exhibits a parabolic dispersion consistent with the Schrödinger approximation [4, 10]. However, for large  $k$ , the dispersion becomes linear, deviating from the Schrödinger model. The degenerate modes split linearly with  $k_i$  for  $k_i \neq 0$ . For example, for  $n = 4$ , they form a chiral dispersion analogous to chiral fermions in three-

dimensional crystals [27] (see Methods and Supp. Fig. S2 for the four-photon dispersion). This analysis lays the groundwork for future studies of  $n > 3$  polaritons.

To summarize, we have analyzed how the spatial symmetry of the wavefunction  $\psi(x_1, \dots, x_n)$  of  $n$  interacting polaritons emerges from its multicomponent structure. We provide analytical models and solutions for multipolariton dispersion and spatial propagation, as well as a full numerical model for three photons describing the evolution in a nonuniform medium and the resulting temporal correlations. By measuring three-photon correlations in a Rydberg polariton system, we experimentally confirm the predicted symmetry of warped vortex rings present in the phase of  $\psi(x_1, x_2, x_3)$ . Thus, we demonstrate experimentally observable effects of strongly interacting polaritons that are not described by traditionally accepted models of interacting particles with parabolic dispersion and contact interactions [12, 17].

The existence of high-order dispersion degeneracies for chiral fermions in three-dimensional solids, extending beyond traditional Dirac or Weyl models, is well established [27, 29, 30]. Here, we show that analogous degeneracies, potentially in even higher dimensions, are intrinsic to the multicomponent interacting polaritons, leading to observable phenomena. We anticipate further fundamental insights in other excitation geometries, such as counter-propagating polaritons, opening new avenues for exploring exotic quantum few-body effects.

## Acknowledgments

We thank Leonid Golub, Ashley Harkavi, and Aditya Prakash for useful discussions. We acknowledge financial support from the Israel Science Foundation (grant No. 3491/21, 1982/22), the US-Israel Binational Science Foundation and US National Science Foundation, the Minerva Foundation with funding from the Federal German Ministry for Education and Research, the Leona M. and Harry B. Helmsley Charitable Trust, the Shimon and Golde Picker - Weizmann Annual Grant, and the Laboratory in Memory of Leon and Blacky Broder.

## METHODS

### Experimental methods

We cool  $^{87}\text{Rb}$  atoms in a magneto-optical trap and transfer them to a far-detuned optical dipole trap (ODT) to increase density and OD. The ODT consists of two 7-Watt 1064-nm beams with  $37^\circ$ -angular separation and 160-MHz frequency difference. The atoms undergo further compression and cooling during the transfer, yielding  $6.5 \times 10^5$  atoms with a Gaussian density profile of  $(1\sigma)$   $30 \times 10 \times 10 \mu\text{m}^3$ . We then optically pump the atoms to the maximal spin state  $|g\rangle = |5S_{1/2}, F=2, m_F=2\rangle$  with 97% efficiency. Throughout the pumping and subsequent stages, the ODT is modulated with a 20  $\mu\text{s}$  period and 50% duty cycle, with optical pumping occurring during the ODT off-time windows.

Probing occurs over the next 0.8 seconds within 40,000 ODT off-time windows. During this period, the atomic

density decreases, reducing the OD from 110 to 20, allowing data collection across this OD range in a single experimental cycle. Rydberg polaritons are generated by pulsing together the probe and control fields, forming the ladder-type level scheme  $|g\rangle - |p\rangle - |s\rangle$ , where  $|p\rangle = |5P_{3/2}, F=3, m_F=3\rangle$  and  $|s\rangle = |100S_{1/2}, J=1/2, m_J=1/2\rangle$ . The probe light exiting the medium is split between four single-photon detectors: 50% is directed to the phase detector  $D_\phi$ , and the remainder is equally split between  $D_1, D_2$ , and  $D_3$  (see Fig. 1a). The probe light reaching  $D_\phi$  is mixed with a local oscillator field shifted by 0.9 MHz. The conditional phase  $\phi^{(3)}$  is extracted from shifts in the detected beat note, correlated with photon pair detections in the other detectors. Further details on the experimental setup and analysis are provided in Ref. [15].

The experiment is conducted with a control Rabi frequency of  $\Omega = 9.5 \pm 0.1$  MHz and a probe photon rate of 0.25 phot/ $\mu\text{s}$ . The probe detuning is  $\Delta = 28.5 \pm 0.03$  MHz, and the decoherence of the ground-Rydberg transition, including laser linewidths, is estimated to be  $\gamma = 0.07$  MHz. The control detuning is  $\Delta_c = -28.90 \pm 0.03$  MHz for the measurement in Fig. 1b, and  $\Delta_c = -27.47 \pm 0.03$  MHz for Fig. 4. Note that throughout this paper, decay rates and Rabi frequencies are given in the half-width convention.

### Numerical model for three interacting polaritons

For the numerical model, we consider a weak coherent state of light,  $\psi(t)$ , impinging on the medium of three-level atoms. The total wavefunction is given by

$$|\psi(t)\rangle = \epsilon|0\rangle + \int_{-\infty}^{+\infty} \sum_{i=1}^3 dx_1 A_i(x_1, t) \hat{a}_i^\dagger(x_1) |0\rangle + \frac{1}{2} \int_{-\infty}^{+\infty} \int_{-\infty}^{+\infty} \sum_{i,j=1}^3 dx_1 dx_2 A_i A_j(x_1, x_2, t) \hat{a}_i^\dagger(x_1) \hat{a}_j^\dagger(x_2) |0\rangle + \frac{1}{3!} \int_{-\infty}^{+\infty} \int_{-\infty}^{+\infty} \int_{-\infty}^{+\infty} \sum_{i,j,k=1}^3 dx_1 dx_2 dx_3 A_i A_j A_k(x_1, x_2, x_3, t) \hat{a}_i^\dagger(x_1) \hat{a}_j^\dagger(x_2) \hat{a}_k^\dagger(x_3) |0\rangle, \quad (7)$$

where  $A = [E, P, S]$ , and the excitation operators are  $\hat{a} = [\hat{\epsilon}, \hat{p}, \hat{s}]$ . We assume  $|\epsilon| \ll 1$  and neglect four or more excitations. As described in the main text, the ground  $|g\rangle$ , excited  $|p\rangle$ , and Rydberg  $|s\rangle$  states are coupled via the level-type scheme

$$|g\rangle \begin{array}{c} \xrightarrow{g, \sqrt{\rho}} \\ \xleftrightarrow{\Delta, \Gamma} \end{array} |p\rangle \begin{array}{c} \xrightarrow{\Omega} \\ \xleftrightarrow{\delta, \gamma} \end{array} |s\rangle,$$

forming Rydberg polaritons. The Hamiltonian governing the single-polariton propagation  $H(x)\psi = 0$ , where  $\psi(x) = [E(x), P(x), S(x)]^T$ , is given by Eq. (1) with parameters defined therein.

The two- and three-polariton wavefunctions  $\psi(x_1, x_2)$  and  $\psi(x_1, x_2, x_3)$  have  $3^2$  and  $3^3$  components, respec-

tively. The effective Hamiltonian for a free three-polariton propagation is thus given by a  $27 \times 27$  matrix constructed from  $H(x)$  as

$$\mathcal{H}(x_1, x_2, x_3) = I \otimes H(x_2) \otimes I + I \otimes I \otimes H(x_3) + H(x_1) \otimes I \otimes I, \quad (8)$$

where  $I$  is the  $3 \times 3$  identity matrix. Additionally, the Rydberg interaction between the polaritons is described by the Hamiltonian

$$\mathcal{V} = \frac{1}{2} \iint dx dx' V_{\text{ss}}(x, x') \hat{S}^\dagger(x') \hat{S}^\dagger(x) \hat{S}(x) \hat{S}(x'), \quad (9)$$

where  $\hat{S}(x)$  is the excitation operator to the Rydberg state, and  $V_{\text{ss}}(x, x') = C_6/|x - x'|^6$  is the Rydberg interaction potential. In our calculations, we project this

Hamiltonian onto the three-polariton space.

We consider an atomic cloud with a Gaussian density

profile  $\rho = \rho(x)$  centered at  $x_o/2 = 5\sigma$ , such that the range  $x \in [0, x_o]$  fully contains the cloud. The equations of motion for the three-photon amplitudes then read:

$$\begin{aligned}
\partial_t EEE &= -c(\partial_{x_1} + \partial_{x_2} + \partial_{x_3})EEE + i\tilde{g}(x_1)PEE + i\tilde{g}(x_2)EPE + i\tilde{g}(x_3)EEP, \\
\partial_t EEP &= -c(\partial_{x_1} + \partial_{x_2})EEP - (\Gamma - i\Delta)EEP + i\tilde{g}(x_1)PEP + i\tilde{g}(x_2)EPP + i\tilde{g}(x_3)EEE + i\Omega EES, \\
\partial_t EES &= -c(\partial_{x_1} + \partial_{x_2})EES - (\gamma - i\delta)EES + i\tilde{g}(x_1)PES + i\tilde{g}(x_2)EPS + i\Omega EEP, \\
\partial_t EPE &= -c(\partial_{x_1} + \partial_{x_3})EPE - (\Gamma - i\Delta)EPE + i\tilde{g}(x_1)PPE + i\tilde{g}(x_2)EEE + i\tilde{g}(x_3)EPP + i\Omega ESE, \\
\partial_t EPP &= -c\partial_{x_1}EPP - 2(\Gamma - i\Delta)EPP + i\tilde{g}(x_1)PPP + i\tilde{g}(x_2)EEP + i\tilde{g}(x_3)EPE + i\Omega EPS + i\Omega ESP, \\
\partial_t EPS &= -c\partial_{x_1}EPS - (\Gamma - i\Delta)EPS - (\gamma - i\delta)EPS + i\tilde{g}(x_1)PPS + i\tilde{g}(x_2)EES + i\Omega EPP + i\Omega ESS, \\
\partial_t ESE &= -c(\partial_{x_1} + \partial_{x_3})ESE - (\gamma - i\delta)ESE + i\tilde{g}(x_1)PSE + i\tilde{g}(x_3)ESP + i\Omega EPE, \\
\partial_t ESP &= -c\partial_{x_1}ESP - (\Gamma - i\Delta)ESP - (\gamma - i\delta)ESP + i\tilde{g}(x_1)PSP + i\tilde{g}(x_3)ESE + i\Omega EPP + i\Omega ESS, \\
\partial_t ESS &= -c\partial_{x_1}ESS - 2(\gamma - i\delta)ESS + i\tilde{g}(x_1)PSS + i\Omega EPS + i\Omega ESP - iV_{ss}(x_2, x_3)ESS, \\
\partial_t PEE &= -c(\partial_{x_2} + \partial_{x_3})PEE - (\Gamma - i\Delta)PEE + i\tilde{g}(x_1)EEE + i\tilde{g}(x_2)PPE + i\tilde{g}(x_3)PEP + i\Omega SEE, \\
\partial_t PEP &= -c\partial_{x_2}PEP - 2(\Gamma - i\Delta)PEP + i\tilde{g}(x_1)EEP + i\tilde{g}(x_2)PPP + i\tilde{g}(x_3)PEE + i\Omega PES + i\Omega SEP, \\
\partial_t PES &= -c\partial_{x_2}PES - (\Gamma - i\Delta)PES - (\gamma - i\delta)PES + i\tilde{g}(x_1)EES + i\tilde{g}(x_2)PPS + i\Omega PEP + i\Omega SES, \\
\partial_t PPE &= -c\partial_{x_3}PPE - 2(\Gamma - i\Delta)PPE + i\tilde{g}(x_1)EPE + i\tilde{g}(x_2)PEE + i\tilde{g}(x_3)PPP + i\Omega PSE + i\Omega SPE, \\
\partial_t PPP &= -3(\Gamma - i\Delta)PPP + i\tilde{g}(x_1)EPP + i\tilde{g}(x_2)PEP + i\tilde{g}(x_3)PPE + i\Omega PPS + i\Omega PSP + i\Omega SPP, \\
\partial_t PPS &= -2(\Gamma - i\Delta)PPS - (\gamma - i\delta)PPS + i\tilde{g}(x_1)EPS + i\tilde{g}(x_2)PES + i\Omega PPP + i\Omega PSS + i\Omega SPS, \\
\partial_t PSE &= -c\partial_{x_3}PSE - (\Gamma - i\Delta)PSE - (\gamma - i\delta)PSE + i\tilde{g}(x_1)ESE + i\tilde{g}(x_3)PSP + i\Omega PPE + i\Omega SSE, \\
\partial_t PSP &= -2(\Gamma - i\Delta)PSP - (\gamma - i\delta)PSP + i\tilde{g}(x_1)ESP + i\tilde{g}(x_3)PSE + i\Omega PPP + i\Omega PSS + i\Omega SSP, \\
\partial_t PSS &= -(\Gamma - i\Delta)PSS - 2(\gamma - i\delta)PSS + i\tilde{g}(x_1)ESS + i\Omega PPS + i\Omega PSP + i\Omega SSS - iV_{ss}(x_2, x_3)PSS, \\
\partial_t SEE &= -c(\partial_{x_2} + \partial_{x_3})SEE - (\gamma - i\delta)SEE + i\tilde{g}(x_2)SPE + i\tilde{g}(x_3)SEP + i\Omega PEE, \\
\partial_t SEP &= -c\partial_{x_2}SEP - (\Gamma - i\Delta)SEP - (\gamma - i\delta)SEP + i\tilde{g}(x_2)SPP + i\tilde{g}(x_3)SEE + i\Omega PEP + i\Omega SES, \\
\partial_t SES &= -c\partial_{x_2}SES - 2(\gamma - i\delta)SES + i\tilde{g}(x_2)SPS + i\Omega PES + i\Omega SEP - iV_{ss}(x_1, x_3)SES, \\
\partial_t SPE &= -c\partial_{x_3}SPE - (\Gamma - i\Delta)SPE - (\gamma - i\delta)SPE + i\tilde{g}(x_2)SEE + i\tilde{g}(x_3)SPP + i\Omega PPE + i\Omega SSE, \\
\partial_t SPP &= -2(\Gamma - i\Delta)SPP - (\gamma - i\delta)SPP + i\tilde{g}(x_2)SEP + i\tilde{g}(x_3)SPE + i\Omega PPP + i\Omega SPS + i\Omega SSP, \\
\partial_t SPS &= -(\Gamma - i\Delta)SPS - 2(\gamma - i\delta)SPS + i\tilde{g}(x_2)SES + i\Omega PPS + i\Omega SPP + i\Omega SSS - iV_{ss}(x_1, x_3)SPS, \\
\partial_t SSE &= -c\partial_{x_3}SSE - 2(\gamma - i\delta)SSE + i\tilde{g}(x_3)SSP + i\Omega PSE + i\Omega SPE - iV_{ss}(x_1, x_2)SSE, \\
\partial_t SSP &= -(\Gamma - i\Delta)SSP - 2(\gamma - i\delta)SSP + i\tilde{g}(x_3)SSE + i\Omega PSP + i\Omega SPP + i\Omega SSS - iV_{ss}(x_1, x_2)SSP, \\
\partial_t SSS &= -3(\gamma - i\delta)SSS + i\Omega PSS + i\Omega SPS + i\Omega SSP - iV_{sss}(x_1, x_2, x_3)SSS.
\end{aligned} \tag{10}$$

Here, the three-body interaction term is defined as  $V_{sss}(x_1, x_2, x_3) = \sum_{i \neq j} V_{ss}(x_i, x_j)$ , and the spatially dependent coupling is given by  $\tilde{g}(x) = g\sqrt{\rho(x)}$ . These 27 equations can be solved to obtain the steady-state three-photon amplitude  $EEE(x_1, x_2, x_3)$  inside the medium, *i.e.*, within the range  $0 < x_{1,2,3} < x_o$ .

To obtain the three-photon steady state, we numerically evolve the system over time until convergence at sufficiently large  $t$ . The evolution is performed hierarchically on the different sections of the  $(x_1, x_2, x_3)$  space in Fig. 2d. We begin by solving for the steady-state wavefunction of a single polariton  $\psi_i(x)$ , with  $i = \{E, P, S\}$ , within the brown sections in Fig. 2d. These solutions

serve as (stationary) boundary conditions for the three light-blue sections [4, 10, 15]. We then compute the two-photon steady-state wavefunction  $\psi_{ij}(x, x')$  within these sections, using the initial condition  $\psi_{ij} = (x_1, x_2, t = 0) = 0$  and solving the nine equations of motion for two interacting polaritons (a reduced form of Eqs. (10), *e.g.*, Eq. (S5) in Ref. [15]). Finally, these solutions are used as boundary conditions for the main (gray) section,

$$\begin{aligned}
\psi_{ijk}(x_1 = 0, x_2, x_3, t) &= \psi_i(x_1 = 0)\psi_{jk}(x_2, x_3), \\
\psi_{ijk}(x_1, x_2 = 0, x_3, t) &= \psi_j(x_2 = 0)\psi_{ik}(x_1, x_3), \\
\psi_{ijk}(x_1, x_2, x_3 = 0, t) &= \psi_k(x_3 = 0)\psi_{ij}(x_1, x_2),
\end{aligned} \tag{11}$$

and we solve Eqs. (10) for the three-photon steady-state amplitude  $\psi_{ijk}(x_1, x_2, x_3)$  with the initial condition  $\psi(x_1, x_2, x_3, t = 0) = 0$ . Examples of these results are shown in Fig. 3.

Having obtained the three-photon wavefunction inside the medium, we proceed to compute the experimentally accessible correlation functions  $g^{(3)}(\tau_1, \tau_2)$  and  $\phi^{(3)}(\tau_1, \tau_2)$ , pertaining to statistics and conditional phase of photons exiting the medium. Here  $\tau_1 = t_2 - t_1$  and  $\tau_2 = t_3 - t_2$  denote the time intervals between successive photon detections ( $t_1 \leq t_2 \leq t_3$ ). To compute these functions, we first evolve the two-photon wavefunction  $\psi_{jk}(x_2, x_3, \tau_1)$  over time  $\tau_1$  after the detection of the first photon at  $x_1 = x_o$ . The initial condition is set as  $\psi_{jk}(x_2, x_3, \tau_1 = 0) = \psi_{Ejk}(x_1 = x_o, x_2, x_3)$  with the boundary condition  $\psi_{jk}(x_2, x_3 = 0, \tau_1) = \psi_{jk}(x_1 = x_o, x_2, \tau_1)$ . Here,  $\psi_{jk}(x_1 = x_o, x_2, \tau_1)$  describe two-photon correlations after the first photon detection. Finally, three-photon correlations (intensity and phase) are obtained by evolving the single photon amplitude over time  $\tau_2$  after the second photon detection at  $x_2 = x_o$ . Further details on these calculations are provided in the Supplementary Materials. Calculation results are shown in Figs. 1c and 4g.

### Numerical Parameters

All numerical calculations in the paper use the following parameters:  $\sqrt{2\pi}\sigma = 75 \mu\text{m}$ ,  $r_b = 15.3 \mu\text{m}$ ,  $\Omega = 9.5 \text{ MHz}$ ,  $\Gamma = 3.03 \text{ MHz}$ ,  $\gamma = 0.07 \text{ MHz}$ ,  $\Delta = 28.5 \text{ MHz}$ ,  $\delta = 1.03 \text{ MHz}$ . The optical depths for the different calculations are: OD=110 for Fig. 1c, OD= 90 ( $\varphi = 2.21\pi$ ,  $\lambda = 2.03$ ) for Fig. 3a, OD= 78 ( $\varphi = 1.92\pi$ ,  $\lambda = 0.42$ ) for Figs. 3b,e, and OD= 115 ( $\varphi = 2.82\pi$ ,  $\lambda = 0.47$ ) for Figs. 3c,f, and OD=50–90 for Fig. 4g.

### Phase diagram parameters

Here, we describe the parameters used for the phase diagram in Fig. 2d. Following Eq. (5) in the main text, we assume that the two-photon interaction is governed by a nearly-square potential  $V^{(2)}(r) = U/(1 + 8r^6/r_b^6)$ , where  $U$  represents the change in the refraction index due to the Rydberg blockade,  $U = \sqrt{2}\rho g^2/(\Delta c)$ , and the (negative) effective mass  $m = -U/(2c)$  arises from single-photon dispersion. The interaction strength is quantified by the parameter  $\lambda = |Um|cr_b^2$  and the interaction duration is quantified by  $\varphi = UL/\sqrt{2}$ . We note that these expressions differ slightly from those in Ref. [15] due to a different choice of rotated coordinates. Here we use  $r = (x_1 - x_2)/\sqrt{2}$  and  $R = (x_1 + x_2)/\sqrt{2}$ , whereas in Ref. [15], the definitions were  $r = x_1 - x_2$  and  $R = (x_1 + x_2)/2$ .

### Analytical multiband model

We now describe the calculation of the band structures in Fig. 2(a,b). We begin by rewriting Eqs. (3) in the

center-of-mass reference frame. For two photons,

$$R = \frac{x_1 + x_2}{\sqrt{2}}, \quad r = \frac{x_1 - x_2}{\sqrt{2}}, \quad k = -i\frac{\partial}{\partial r}, \quad (12)$$

which transforms the wavefunction equation into

$$-\frac{i}{\sqrt{2}}\frac{\partial}{\partial R}\psi = \frac{1}{\sqrt{2}}\begin{pmatrix} -k & 0 \\ 0 & k \end{pmatrix}\psi - \frac{\tilde{\omega}_D}{c}\psi + \frac{\omega_D}{2c}\begin{pmatrix} 1 & 1 \\ 1 & 1 \end{pmatrix}\psi, \quad (13)$$

where  $\omega_D \equiv V_2(\infty) = \rho g^2/\Delta \equiv$ . Replacing  $(-i/2)\partial_R$  by  $K$  in Eq. (13) and diagonalize the matrix, we obtain

$$K_{\pm}(k) = -\frac{\sqrt{2}\tilde{\omega}_D}{c} + \frac{\sqrt{2}\omega_D}{2c} \pm \sqrt{\frac{1}{2}\left(\frac{\omega_D}{c}\right)^2 + k^2}. \quad (14)$$

For small  $k$ , the dispersion is parabolic,

$$K_+(k) = K_+(k=0) + \frac{ck^2}{\sqrt{2}\omega_D}, \quad (15)$$

corresponding to an effective mass  $m = \omega_D/(\sqrt{2}c)$ . The results obtained from Eqs. (14),(15) are shown in Fig. 2a.

For three photons, we employ the Jacobi coordinates to clearly separate center-of-mass motion from internal relative motion,

$$R = \frac{x_1 + x_2 + x_3}{\sqrt{3}}, \quad \eta = \frac{x_1 - x_2}{\sqrt{2}}, \quad \zeta = \frac{x_1 + x_2 - 2x_3}{\sqrt{6}}, \\ K = -i\partial_R, \quad k_\eta = -i\partial_\eta, \quad k_\zeta = -i\partial_\zeta, \quad (16)$$

yielding the three-photon dispersion equation

$$-\frac{i}{\sqrt{3}}\frac{\partial}{\partial R}\psi = \frac{\sqrt{6}}{3}\begin{pmatrix} -\frac{1}{2}k_\zeta - \frac{\sqrt{3}}{2}k_\eta & 0 & 0 \\ 0 & -\frac{1}{2}k_\zeta + \frac{\sqrt{3}}{2}k_\eta & 0 \\ 0 & 0 & k_\zeta \end{pmatrix}\psi \\ -\frac{\tilde{\omega}_D}{c}\psi + \frac{\omega_D}{3c}\begin{pmatrix} 1 & 1 & 1 \\ 1 & 1 & 1 \\ 1 & 1 & 1 \end{pmatrix}\psi. \quad (17)$$

Transforming to the basis  $ESS_+ = (ESS + SES + SSE)/\sqrt{3}$ ,  $ESS_- = (ESS - SES)/\sqrt{2}$ ,  $ESS'_- = (ESS + SES - 2SSE)/\sqrt{6}$ , Eq. (17) simplifies to

$$-\frac{i}{\sqrt{3}}\frac{\partial}{\partial R}\psi = -\frac{1}{\sqrt{3}}\begin{pmatrix} 0 & k_\eta & k_\zeta \\ k_\eta & k_\zeta/\sqrt{2} & k_\eta/\sqrt{2} \\ k_\zeta & k_\eta/\sqrt{2} & -k_\zeta/\sqrt{2} \end{pmatrix}\psi \\ -\frac{\tilde{\omega}_D}{c}\psi + \frac{\omega_D}{c}\begin{pmatrix} 1 & 0 & 0 \\ 0 & 0 & 0 \\ 0 & 0 & 0 \end{pmatrix}\psi. \quad (18)$$

We use this equation to compute the band structure in Fig. 2b.

Replacing  $-i\partial_R$  by  $K$  in Eq. (17), we find for the

parabolic band at small  $k$ :

$$K(\vec{k}) = -\frac{\sqrt{3}\tilde{\omega}_D}{c} + \frac{\sqrt{3}\omega_D}{c} + \frac{1}{\sqrt{3}} \frac{ck^2}{\omega_D}. \quad (19)$$

The two other bands form a Dirac cone,

$$K = -\sqrt{3} \frac{\tilde{\omega}_D}{c} \pm \frac{|k|}{\sqrt{2}}, \quad \text{where } k \equiv \sqrt{k_\eta^2 + k_\zeta^2}. \quad (20)$$

The corresponding band structure is plotted in Fig. 2b.

### Extension to $n > 3$ photons

For  $n > 3$  photons, we extend the  $n$ -component wavefunction  $\psi$ , where each component corresponds to a single propagating photon with the remaining excitations in the Rydberg states. For instance, for  $n = 4$ , we define  $\psi = [ESSS, SESS, SSES, SSSE]$ . The explicit form of the 4-photon Hamiltonian a straightforward generalization of Eqs. (8) and (9):

$$\begin{aligned} \mathcal{H}(x_1 \dots x_4) &= H(x_1) \otimes I \otimes I \otimes I \\ &+ I \otimes H(x_2) \otimes I \otimes I + \dots + I \otimes I \otimes I \otimes H(x_4). \end{aligned} \quad (21)$$

After eliminating the  $SSSS$  state, we recover Eq. (6) in the main text,

$$i \frac{\partial \psi_i}{\partial t} = -ic \frac{\partial \psi_i}{\partial x_i} + \tilde{\omega}_D \psi_i + \frac{1}{n} V_n(x_1, \dots, x_n) \sum_{i=1}^n \psi_i, \quad (22)$$

with  $V_n$  given by Eq. (4). This procedure applies for any number  $n > 4$  of photons.

We now consider the stationary case for  $n = 4$  photons and assume that they are sufficiently far apart so that  $V_n \equiv \omega_D$ . Using the center-of-mass reference frame and the generalized Jacobi coordinates [31], we define

$$\begin{aligned} R &= \frac{x_1 + x_2 + x_3 + x_4}{2}, \\ \eta_1 &= \frac{x_1 - x_2}{\sqrt{2}}, \eta_2 = \frac{x_3 - x_4}{\sqrt{2}}, \eta_3 = \frac{x_1 + x_2 - x_3 - x_4}{2}. \end{aligned} \quad (23)$$

The four-photon dispersion equation then becomes

$$\begin{aligned} -\frac{i}{2} \frac{\partial}{\partial R} \psi & \\ &= \begin{pmatrix} \frac{1}{\sqrt{2}} \kappa_1 + \frac{1}{2} \kappa_3 & 0 & 0 & 0 \\ 0 & -\frac{1}{\sqrt{2}} \kappa_1 + \frac{1}{2} \kappa_3 & 0 & 0 \\ 0 & 0 & \frac{1}{\sqrt{2}} \kappa_2 - \frac{1}{2} \kappa_3 & 0 \\ 0 & 0 & 0 & -\frac{1}{\sqrt{2}} \kappa_2 - \frac{1}{2} \kappa_3 \end{pmatrix} \psi \\ &- \frac{\tilde{\omega}_D}{c} \psi + \frac{\omega_D}{4c} \begin{pmatrix} 1 & 1 & 1 & 1 \\ 1 & 1 & 1 & 1 \\ 1 & 1 & 1 & 1 \\ 1 & 1 & 1 & 1 \end{pmatrix} \psi, \end{aligned} \quad (24)$$

where the relative motion wavevectors are  $\kappa_i = -i\partial_{\eta_i}$  and  $-i\partial_R \equiv K$ . The massive eigenstate of Eq. (24) cor-

responds to

$$K = -2 \frac{\tilde{\omega}_D}{c} - \frac{c\kappa^2}{2\omega_D}. \quad (25)$$

The results of the calculation are presented in Supplementary Fig. S2. The dispersion exhibits similarities to Fig. 2b in the main text for  $n = 3$  photons. However, in this case, we observe a warped cone (blue) with a 4-fold rotational symmetry rather than a 3-fold one. Additionally, a more complex three-fold degeneracy (red bands) emerges, which splits for  $\kappa < 0$ .

### Propagation of three polaritons

The Dirac-like equation model introduced above also describes the propagation of interacting polaritons, yielding the results in Fig. 2(f,h,i). Here, we outline the calculation technique for three photons.

We solve Eq. (18) for  $\psi(\eta, \zeta, R)$  with the initial condition  $\psi(\eta, \zeta, R = 0) = [1, 0, 0]^T$ . The wavefunction is represented as

$$\psi(\eta, \zeta, R) = \sum_{\mathbf{b}} \psi_{\mathbf{b}}(R) e^{i(b_\eta \eta + b_\zeta \zeta)}, \quad (26)$$

where  $\mathbf{b}$  are the reciprocal lattice vectors, defined as

$$\mathbf{b}_{nm} = n\mathbf{b}_1 + m\mathbf{b}_2, \quad (27)$$

$$\mathbf{b}_1 = \frac{2\pi D}{S} \mathbf{e}_1, \quad \mathbf{b}_2 = \frac{2\pi D}{S} \left( \frac{1}{2} \mathbf{e}_1 + \frac{\sqrt{3}}{2} \mathbf{e}_2 \right). \quad (28)$$

Here,  $n, m$  are integers,  $\mathbf{e}_{1,2}$  are Cartesian basis vectors,  $D \gg r_b$  is the lattice period, and  $S = \sqrt{3}D^2/2$  is unit cell area in real space. The numerical calculation in Fig. 2(g-i) has been performed taking into account 1069 vectors  $\mathbf{b}$  and  $D = 120r_b$ . Using this representation, Eq. (18) is transformed into a system of  $3N$  linear equations, where  $N$  is the chosen number of basis states,

$$\begin{aligned} i \frac{\partial}{\partial R} \psi_{\mathbf{b}} &= \begin{pmatrix} 0 & b_\eta & b_\zeta \\ b_\eta & b_\zeta/\sqrt{2} & b_\eta/\sqrt{2} \\ b_\zeta & b_\eta/\sqrt{2} & -b_\zeta/\sqrt{2} \end{pmatrix} \psi_{\mathbf{b}} \\ &+ \frac{\sqrt{3}\tilde{\omega}_D}{c} \psi_{\mathbf{b}} - \sum_{\mathbf{b}'} \frac{\sqrt{3}V_{3,\mathbf{b}-\mathbf{b}'}}{c} \begin{pmatrix} 1 & 0 & 0 \\ 0 & 0 & 0 \\ 0 & 0 & 0 \end{pmatrix} \psi_{\mathbf{b}'}. \end{aligned} \quad (29)$$

Here,

$$V_{3,\mathbf{b}-\mathbf{b}'} = \frac{1}{S} \iint d\eta d\zeta e^{-i(b_\eta \eta + b_\zeta \zeta)} V_3(\eta, \zeta) \quad (30)$$

is the Fourier component of the interaction potential. Following Eq. (19), the Schrödinger equation approximation is obtained by replacing Eq. (29) with the single-

band model for a single scalar amplitude  $\psi_{\mathbf{b}}$ :

$$i \frac{\partial}{\partial R} \psi_{\mathbf{b}} = -\frac{c}{\sqrt{3}\omega_D} (b_{\eta}^2 + b_{\zeta}^2) \psi_{\mathbf{b}} + \frac{\sqrt{3}\tilde{\omega}_D}{c} \psi_{\mathbf{b}} - \sum_{\mathbf{b}'} \frac{\sqrt{3}V_{3,\mathbf{b}-\mathbf{b}'}}{c} \psi_{\mathbf{b}'}. \quad (31)$$

We diagonalize Eq. (29) to find the eigenvectors  $\psi_{\nu}^{(\mathbf{b})}(R) \propto e^{iK_{\nu}R}$  with the corresponding eigenvalues  $K_{\nu}$ . The solution is then expressed as

$$\psi(\eta, \zeta, R) = \sum_{\mathbf{b}, \nu} e^{iK_{\nu}R} e^{i(b_{\eta}\eta + b_{\zeta}\zeta)} \psi_{\mathbf{b}}^{(\nu)} \langle \nu | 0 \rangle, \quad (32)$$

where  $\langle \nu | 0 \rangle = [\psi_0^{(\nu)}]_1 \delta_{\mathbf{b},1}$  is the overlap of the eigenvector with the homogeneous initial solution.

- 
- [1] C. Murray and T. Pohl, Quantum and Nonlinear Optics in Strongly Interacting Atomic Ensembles, in *Advances In Atomic, Molecular, and Optical Physics*, Vol. 65 (Academic Press, Cambridge, MA, USA, 2016) pp. 321–372.
- [2] O. Firstenberg, C. S. Adams, and S. Hofferberth, Nonlinear quantum optics mediated by Rydberg interactions, *J. Phys. B: At. Mol. Opt. Phys.* **49**, 152003 (2016).
- [3] D. E. Chang, V. Vuletić, and M. D. Lukin, Quantum nonlinear optics — photon by photon, *Nat. Photonics* **8**, 685 (2014).
- [4] T. Peyronel, O. Firstenberg, Q.-Y. Liang, S. Hofferberth, A. V. Gorshkov, T. Pohl, M. D. Lukin, and V. Vuletić, Quantum nonlinear optics with single photons enabled by strongly interacting atoms, *Nature* **488**, 57 (2012).
- [5] H. Gorniaczyk, C. Tresp, J. Schmidt, H. Fedder, and S. Hofferberth, Single-Photon Transistor Mediated by Interstate Rydberg Interactions, *Phys. Rev. Lett.* **113**, 053601 (2014).
- [6] S. Baur, D. Tiarks, G. Rempe, and S. Dürr, Single-Photon Switch Based on Rydberg Blockade, *Physical Review Letters* **112**, 073901 (2014).
- [7] D. P. Ornelas-Huerta, P. Bienias, A. N. Craddock, M. J. Gullans, A. J. Hachtel, M. Kalinowski, M. E. Lyon, A. V. Gorshkov, S. L. Rolston, and J. V. Porto, Tunable three-body loss in a nonlinear Rydberg medium, *Phys. Rev. Lett.* **126**, 173401 (2021).
- [8] D. Tiarks, S. Schmidt, G. Rempe, and S. Dürr, Optical  $\pi$  phase shift created with a single-photon pulse, *Sci. Adv.* **2**, e1600036 (2016).
- [9] J. D. Thompson, T. L. Nicholson, Q.-Y. Liang, S. H. Cantu, A. V. Venkatramani, S. Choi, I. A. Fedorov, D. Viscor, T. Pohl, M. D. Lukin, and V. Vuletić, Symmetry-protected collisions between strongly interacting photons, *Nature* **542**, 206 (2017).
- [10] O. Firstenberg, T. Peyronel, Q.-Y. Liang, A. V. Gorshkov, M. D. Lukin, and V. Vuletić, Attractive photons in a quantum nonlinear medium, *Nature* **502**, 71 (2013).
- [11] N. Stiesdal, J. Kumlin, K. Kleinbeck, P. Lunt, C. Braun, A. Paris-Mandoki, C. Tresp, H. P. Büchler, and S. Hofferberth, Observation of three-body correlations for photons coupled to a Rydberg superatom, *Phys. Rev. Lett.* **121**, 103601 (2018).
- [12] Q.-Y. Liang, A. V. Venkatramani, S. H. Cantu, T. L. Nicholson, M. J. Gullans, A. V. Gorshkov, J. D. Thompson, C. Chin, M. D. Lukin, and V. Vuletić, Observation of three-photon bound states in a quantum nonlinear medium, *Science* **359**, 783 (2018).
- [13] H. Busche, P. Huillery, S. W. Ball, T. Ilieva, M. P. A. Jones, and C. S. Adams, Contactless nonlinear optics mediated by long-range Rydberg interactions, *Nat. Phys.* **13**, 655 (2017).
- [14] L. W. Clark, N. Jia, N. Schine, C. Baum, A. Georgakopoulos, and J. Simon, Interacting Floquet polaritons, *Nature* **571**, 532 (2019).
- [15] L. Drori, B. C. Das, T. D. Zohar, G. Winer, E. Poem, A. Poddubny, and O. Firstenberg, Quantum vortices of strongly interacting photons, *Science* **381**, 193 (2023).
- [16] K. Jachymski, P. Bienias, and H. P. Büchler, Three-body interaction of Rydberg slow-light polaritons, *Phys. Rev. Lett.* **117**, 053601 (2016).
- [17] M. J. Gullans, J. D. Thompson, Y. Wang, Q.-Y. Liang, V. Vuletić, M. D. Lukin, and A. V. Gorshkov, Effective field theory for Rydberg polaritons, *Phys. Rev. Lett.* **117**, 113601 (2016).
- [18] A. Grankin, P. Grangier, and E. Brion, Diagrammatic treatment of few-photon scattering from a Rydberg-blockaded atomic ensemble in a cavity, *Phys. Rev. A* **98**, 053860 (2018).
- [19] M. Kalinowski, Y. Wang, P. Bienias, M. J. Gullans, D. P. Ornelas-Huerta, A. N. Craddock, S. L. Rolston, J. V. Porto, H. P. Büchler, and A. V. Gorshkov, Resonant enhancement of three-body loss between strongly interacting photons, *Phys. Rev. Res.* **4**, L022059 (2022).
- [20] T. Caneva, M. T. Manzoni, T. Shi, J. S. Douglas, J. I. Cirac, and D. E. Chang, Quantum dynamics of propagating photons with strong interactions: a generalized input–output formalism, *New J. Phys.* **17**, 113001 (2015).
- [21] Z. Chen, Y. Zhou, and J.-T. Shen, Correlation signatures for a coherent three-photon scattering in waveguide quantum electrodynamics, *Opt. Lett.* **45**, 2559 (2020).
- [22] A. S. Sheremet, M. I. Petrov, I. V. Iorsh, A. V. Poshakinskiy, and A. N. Poddubny, Waveguide quantum electrodynamics: Collective radiance and photon-photon correlations, *Rev. Mod. Phys.* **95**, 015002 (2023).
- [23] G. Calajó and D. E. Chang, Emergence of solitons from many-body photon bound states in quantum nonlinear media, *Phys. Rev. Res.* **4**, 023026 (2022).
- [24] A. Denisov, H. M. Castro-Beltran, and H. J. Carmichael, Time-asymmetric fluctuations of light and the breakdown of detailed balance, *Phys. Rev. Lett.* **88**, 243601 (2002).
- [25] M. Koch, C. Sames, M. Balbach, H. Chibani, A. Kubanek, K. Murr, T. Wilk, and G. Rempe, Three-photon correlations in a strongly driven atom-cavity system, *Phys. Rev. Lett.* **107**, 023601 (2011).
- [26] A. V. Gorshkov, J. Otterbach, M. Fleischhauer, T. Pohl, and M. D. Lukin, Photon-Photon Interactions via Rydberg Blockade, *Phys. Rev. Lett.* **107**, 133602 (2011).
- [27] B. Bradlyn, J. Cano, Z. Wang, M. G. Vergniory, C. Felser, R. J. Cava, and B. A. Bernevig, Beyond Dirac and Weyl fermions: Unconventional quasiparticles in conventional crystals, *Science* **353**, aaf5037 (2016).
- [28] P. Bienias, S. Choi, O. Firstenberg, M. F. Maghrebi, M. Gullans, M. D. Lukin, A. V. Gorshkov, and H. P. Büchler, Scattering resonances and bound states for strongly interacting Rydberg polaritons, *Phys. Rev. A*

- 90**, 053804 (2014).
- [29] M. Orlita, D. M. Basko, M. S. Zholudev, F. Teppe, W. Knap, V. I. Gavrilenko, N. N. Mikhailov, S. A. Dvoretzkii, P. Neugebauer, C. Faugeras, A.-L. Barra, G. Martinez, and M. Potemski, Observation of three-dimensional massless Kane fermions in a zinc-blende crystal, *Nature Physics* **10**, 233 (2014).
- [30] Z. Rao, H. Li, T. Zhang, S. Tian, C. Li, B. Fu, C. Tang, L. Wang, Z. Li, W. Fan, J. Li, Y. Huang, Z. Liu, Y. Long, C. Fang, H. Weng, Y. Shi, H. Lei, Y. Sun, T. Qian, and H. Ding, Observation of unconventional chiral fermions with long Fermi arcs in CoSi, *Nature* **567**, 496 (2019).
- [31] J. Leroy and R. Wallace, Procedures leading to a variety of orthonormal Jacobi-type coordinates of relevance to large-amplitude vibration and scattering problems, *Chem. Phys.* **111**, 11 (1987).

## Supplementary Information

### Multiband dispersion and warped vortices of strongly-interacting photons

Bankim Chandra Das *et al.*

#### Computing temporal detection statistics in simulations

##### (a) Two photons

We assume the detectors are positioned immediately outside the medium, at  $x = x_o$ . For a uniform medium extending from 0 to  $L$ , choose  $x_o = L$ ; for our Gaussian cloud, we choose  $x_o = 10\sigma$ . We further assume a steady state, so that the correlation function  $g^{(2)}(t_1, t_2) = g^{(2)}(\tau)$  is only a function of  $\tau = t_2 - t_1$ . As explained in Methods, the steady state is calculated by numerically integrating the equations of motion up to some long time  $t = t_\infty$ . We then define

$$g^{(2)}(\tau) \equiv g^{(2)}(x_o, x_o, t_\infty, t_\infty + \tau) = \frac{\langle \psi | \epsilon^\dagger(x_o, t_\infty) \epsilon^\dagger(x_o, t_\infty + \tau) \epsilon(x_o, t_\infty + \tau) \epsilon(x_o, t_\infty) | \psi \rangle}{\langle \psi | \epsilon^\dagger(x_o, t_\infty) \epsilon(x_o, t_\infty) | \psi \rangle \langle \psi | \epsilon^\dagger(x_o, t_\infty) \epsilon(x_o, t_\infty) | \psi \rangle}, \quad (\text{S1})$$

where we already assumed the two terms in the denominator to be the same (independent of  $t$ ) at steady state. The denominator can be calculated from the single-photon amplitude,

$$\langle \psi | \epsilon^\dagger(x_o, t_\infty) \epsilon(x_o, t_\infty) | \psi \rangle \langle \psi | \epsilon^\dagger(x_o, t_\infty) \epsilon(x_2, t_2) | \psi \rangle = |E(x_o)|^4, \quad (\text{S2})$$

where  $E(x_o)$  is the the one-photon steady-state solution (the solution at  $t = t_\infty$ ).

We can rewrite the numerator of Eq. (S1) in the following way

$$\langle \psi | \epsilon^\dagger(x_o, t_\infty) \epsilon^\dagger(x_o, t_\infty + \tau) \epsilon(x_o, t_\infty + \tau) \epsilon(x_o, t_\infty) | \psi \rangle = \langle \psi(t_\infty) | \epsilon^\dagger(x_o) e^{i\mathcal{H}(\tau)} \epsilon^\dagger(x_o) \epsilon(x_o) e^{-i\mathcal{H}(\tau)} \epsilon(x_o) | \psi(t_\infty) \rangle. \quad (\text{S3})$$

Here  $\mathcal{H}$  is the effective two-photon Hamiltonian. We write

$$\epsilon(x_o) | \psi(t_\infty) \rangle = E(x_o) | 0 \rangle + \int_{-\infty}^{\infty} dx_2 EE(x_o, x_2) \epsilon^\dagger(x_2) | 0 \rangle + \int_{-\infty}^{\infty} dx_2 EP(x_o, x_2) p^\dagger(x_2) | 0 \rangle + \int_{-\infty}^{\infty} dx_2 ES(x_o, x_2) s^\dagger(x_2) | 0 \rangle \quad (\text{S4})$$

and

$$e^{-i\mathcal{H}(\tau)} \epsilon(x_o) | \psi(t_\infty) \rangle = E(x_o, \tau) | 0 \rangle + \int_{-\infty}^{\infty} dx_2 e^{(2)}(x_o, x_2, \tau) \epsilon^\dagger(x_2) | 0 \rangle + \int_{-\infty}^{\infty} dx_2 p^{(2)}(x_o, x_2, \tau) p^\dagger(x_2) | 0 \rangle + \int_{-\infty}^{\infty} dx_2 s^{(2)}(x_o, x_2, \tau) s^\dagger(x_2) | 0 \rangle. \quad (\text{S5})$$

These  $e^{(2)}(x_o, x_2, \tau)$ ,  $p^{(2)}(x_o, x_2, \tau)$ , and  $s^{(2)}(x_o, x_2, \tau)$  amplitudes obey the equations of motion for a single photon. We solve for the propagation of the second photon after the first photon is detected, which describes the process of measuring the  $g^{(2)}$ . The propagation equation requires the following initial and boundary conditions:

$$\begin{aligned} e^{(2)}(x_o, x_2, \tau = 0) &= EE(x_o, x_2), \\ p^{(2)}(x_o, x_2, \tau = 0) &= EP(x_o, x_2), \\ s^{(2)}(x_o, x_2, \tau = 0) &= ES(x_o, x_2), \\ e^{(2)}(x_o, x_2 = 0, \tau) &= EE(x_o, x_2 = 0). \end{aligned} \quad (\text{S6})$$

Here  $EE$ ,  $EP$ ,  $ES$  are the steady-state two-photon amplitudes. The numerator becomes

$$\langle \psi | \epsilon^\dagger(x_o, t_\infty) \epsilon^\dagger(x_o, t_\infty + \tau) \epsilon(x_o, t_\infty + \tau) \epsilon(x_1, t_1) | \psi \rangle = |e^{(2)}(x_o, x_o, \tau)|^2. \quad (\text{S7})$$

The value of  $g^{(2)}(\tau)$  can then be calculated from Eqs. (S2) and (S7), that is  $g^{(2)}(\tau) = \left| \frac{e^{(2)}(x_o, x_o, \tau)}{E(x_o)E(x_o)} \right|^2$ . The derivation of  $\phi^{(2)}(\tau)$  is similar, and we obtain  $\phi^{(2)}(\tau) = \arg \left[ \frac{e^{(2)}(x_o, x_o, \tau)}{E(x_o)E(x_o)} \right]$ .

### (b) Three photons

We adopt the same assumptions as above and define the three-photon correlation function  $g^{(3)}(\tau_1, \tau_2)$  for  $\tau_1 = t_2 - t_1$  and  $\tau_2 = t_3 - t_2$  ( $t_1 \leq t_2 \leq t_3$ ) as

$$\begin{aligned} g^3(\tau_1, \tau_2) &\equiv g^{(3)}(x_o, x_o, x_o, t_\infty, t_\infty + \tau_1, t_\infty + \tau_2) \\ &= \frac{\langle \psi | \epsilon^\dagger(x_o, t_\infty) \epsilon^\dagger(x_o, t_\infty + \tau_1) \epsilon^\dagger(x_o, t_\infty + \tau_2) \epsilon(x_o, t_\infty + \tau_2) \epsilon(x_o, t_\infty + \tau_1) \epsilon(x_o, t_\infty) | \psi \rangle}{\langle \psi | \epsilon^\dagger(x_o, t_\infty) \epsilon(x_o, t_\infty) | \psi \rangle \langle \psi | \epsilon^\dagger(x_o, t_\infty) \epsilon(x_o, t_\infty) | \psi \rangle \langle \psi | \epsilon^\dagger(x_o, t_\infty) \epsilon(x_o, t_\infty) | \psi \rangle}. \end{aligned} \quad (\text{S8})$$

The denominator can be calculated from the steady-state solution of the single photon amplitude,

$$\langle \psi | \epsilon^\dagger(x_o, t_\infty) \epsilon(x_o, t_\infty) | \psi \rangle \langle \psi | \epsilon^\dagger(x_o, t_\infty) \epsilon(x_o, t_\infty) | \psi \rangle \langle \psi | \epsilon^\dagger(x_o, t_\infty) \epsilon(x_o, t_\infty) | \psi \rangle = |E(x_o)|^6. \quad (\text{S9})$$

For the numerator, we follow the same procedure as above,

$$\begin{aligned} &\langle \psi | \epsilon^\dagger(x_o, t_\infty) \epsilon^\dagger(x_o, t_\infty + \tau_1) \epsilon^\dagger(x_o, t_\infty + \tau_2) \epsilon(x_o, t_\infty + \tau_2) \epsilon(x_o, t_\infty + \tau_1) \epsilon(x_o, t_\infty) | \psi \rangle \\ &= \langle \psi(t_\infty) | \epsilon^\dagger(x_o) e^{i\mathcal{H}\tau_1} \epsilon^\dagger(x_o) e^{i\mathcal{H}\tau_2} \epsilon^\dagger(x_o) \epsilon(x_o) e^{-i\mathcal{H}\tau_2} \epsilon(x_o) e^{-i\mathcal{H}\tau_1} \epsilon(x_o) | \psi(t_\infty) \rangle. \end{aligned} \quad (\text{S10})$$

To calculate

$$e^{-i\mathcal{H}\tau_2} \epsilon(x_o) e^{-i\mathcal{H}\tau_1} \epsilon(x_o) | \psi(t_\infty) \rangle, \quad (\text{S11})$$

we use Eq. (7) to write

$$\begin{aligned} \epsilon(x_o) \psi(t_\infty) &= E(x_o) |0\rangle + \int_{-\infty}^{+\infty} \sum_{i=1}^3 dx_2 E A_i(x_o, x_2) a_i^\dagger(x_2) |0\rangle \\ &+ \iint_{-\infty}^{+\infty} \sum_{i,j=1}^3 dx_2 dx_3 E A_i A_j(x_o, x_2, x_3) a_i^\dagger(x_2) a_j^\dagger(x_3) |0\rangle. \end{aligned} \quad (\text{S12})$$

We now propagate this state in time

$$\begin{aligned} e^{-i\mathcal{H}\tau_1} \epsilon(x_o) \psi(t_\infty) &= E(x_o, \tau_1) |0\rangle + \int_{-\infty}^{+\infty} \sum_i dx_2 e a_i(x_o, x_2, \tau_1) a_i^\dagger(x_2) |0\rangle \\ &+ \iint_{-\infty}^{+\infty} \sum_{i,j=1}^3 dx_2 dx_3 E A_i A_j(x_o, x_2, x_3, \tau_1) a_i^\dagger(x_2) a_j^\dagger(x_3) |0\rangle \end{aligned} \quad (\text{S13})$$

and apply the annihilation operator  $\epsilon(x_o)$  as follows

$$\epsilon(x_o) e^{-i\mathcal{H}\tau_1} \epsilon(x_o) \psi(t_\infty) = e e(x_o, x_2, \tau_1) |0\rangle + \int_{-\infty}^{+\infty} \sum_{i=1}^3 dx_3 a_i(x_o, x_o, x_3, \tau_1) a_i^\dagger(x_3) |0\rangle. \quad (\text{S14})$$

The second propagation in time leads to

$$\begin{aligned} e^{-i\mathcal{H}\tau_2} \epsilon(x_o) e^{-i\mathcal{H}\tau_1} \epsilon(x_o) \psi(t_\infty) &= e e(x_o, x_o, \tau_1, \tau_2) |0\rangle + \int_{-\infty}^{+\infty} dx_3 e(x_o, x_o, x_3, \tau_1, \tau_2) \epsilon^\dagger(x_3) |0\rangle \\ &+ \int_{-\infty}^{+\infty} dx_3 p(x_o, x_o, x_3, \tau_1, \tau_2) p^\dagger(x_3) |0\rangle \\ &+ \int_{-\infty}^{+\infty} dx_3 s(x_o, x_o, x_3, \tau_1, \tau_2) s^\dagger(x_3) |0\rangle. \end{aligned} \quad (\text{S15})$$

The amplitudes  $e(x_o, x_o, x_3, \tau_1, \tau_2)$ ,  $p(x_o, x_o, x_3, \tau_1, \tau_2)$ , and  $s(x_o, x_o, x_3, \tau_1, \tau_2)$  are governed by the one-photon propagation equation, with the following initial condition

$$\begin{aligned} e(x_o, x_o, x_3, \tau_1, 0) &= e e(x_o, x_3, \tau_1), \\ p(x_o, x_o, x_3, \tau_1, 0) &= e p(x_o, x_3, \tau_1), \\ s(x_o, x_o, x_3, \tau_1, 0) &= e s(x_o, x_3, \tau_1). \end{aligned} \quad (\text{S16})$$

Similarly, the boundary conditions are

$$\begin{aligned} e(x_o, x_o, x_3 = 0, \tau_1, \tau_2) &= ee(x_o, 0, \tau_1), \\ p(x_o, x_o, x_3 = 0, \tau_1, \tau_2) &= ep(x_o, 0, \tau_1), \\ s(x_o, x_o, x_3 = 0, \tau_1, \tau_2) &= es(x_o, 0, \tau_1). \end{aligned} \quad (\text{S17})$$

To find the values of  $ee(x_2, x_3, \tau_1)$ ,  $ep(x_2, x_3, \tau_1)$ , and  $es(x_2, x_3, \tau_1)$ , we need to solve the two-photon propagation equations [15] with the initial conditions obtained from the three-photon steady-state solution of Eq. (10):

$$\begin{aligned} ee(x_2, x_3, \tau_1 = 0) &= EEE(x_o, x_2, x_3), \\ ep(x_2, x_3, \tau_1 = 0) &= EEP(x_o, x_2, x_3), \\ es(x_2, x_3, \tau_1 = 0) &= EES(x_o, x_2, x_3), \\ pe(x_2, x_3, \tau_1 = 0) &= EPE(x_o, x_2, x_3), \\ pp(x_2, x_3, \tau_1 = 0) &= EPP(x_o, x_2, x_3), \\ ps(x_2, x_3, \tau_1 = 0) &= EPS(x_o, x_2, x_3), \\ se(x_2, x_3, \tau_1 = 0) &= ESE(x_o, x_2, x_3), \\ sp(x_2, x_3, \tau_1 = 0) &= ESP(x_o, x_2, x_3), \\ ss(x_2, x_3, \tau_1 = 0) &= ESS(x_o, x_2, x_3). \end{aligned} \quad (\text{S18})$$

Similarly, the boundary condition are

$$\begin{aligned} ee(x_2, 0, \tau_1) &= e^{(2)}(x_o, x_2, \tau_1), \\ ee(0, x_3, \tau_1) &= e^{(2)}(x_o, x_3, \tau_1), \\ ep(0, x_3, \tau_1) &= p^{(2)}(x_o, x_3, \tau_1), \\ es(0, x_3, \tau_1) &= s^{(2)}(x_o, x_3, \tau_1), \\ pe(x_2, 0, \tau_1) &= p^{(2)}(x_o, x_2, \tau_1), \\ se(x_2, 0, \tau_1) &= s^{(2)}(x_o, x_2, \tau_1). \end{aligned} \quad (\text{S19})$$

Effectively, this is a time-dependent boundary condition, as it describes the two-photon propagation conditioned on the first-photon detection. The numerator then becomes

$$\langle \psi | \epsilon^\dagger(x_o, t_\infty) \epsilon^\dagger(x_o, t_\infty + \tau_1) \epsilon^\dagger(x_o, t_\infty + \tau_2) \epsilon(x_o, t_\infty + \tau_2) \epsilon(x_o, t_\infty + \tau_1) \epsilon(x_o, t_\infty) | \psi \rangle = |e(x_o, x_o, x_o, \tau_1, \tau_2)|^2. \quad (\text{S20})$$

We calculate  $g^{(3)}(\tau_1, \tau_2)$  from Eq. (S9) and Eq. (S20), that is  $g^{(3)}(\tau_1, \tau_2) = \left| \frac{e(x_o, x_o, x_o, \tau_1, \tau_2)}{E(x_o)E(x_o)E(x_o)} \right|^2$ . The derivation of  $\phi^{(3)}(\tau_1, \tau_2)$  is similar, and we obtain  $\phi^{(3)}(\tau_1, \tau_2) = \arg \left[ \frac{e(x_o, x_o, x_o, \tau_1, \tau_2)}{E(x_o)E(x_o)E(x_o)} \right]$ .

An example of calculated  $g^{(3)}(\tau_1, \tau_2)$  and  $\phi^{(3)}(\tau_1, \tau_2)$  is shown in Fig. S1.

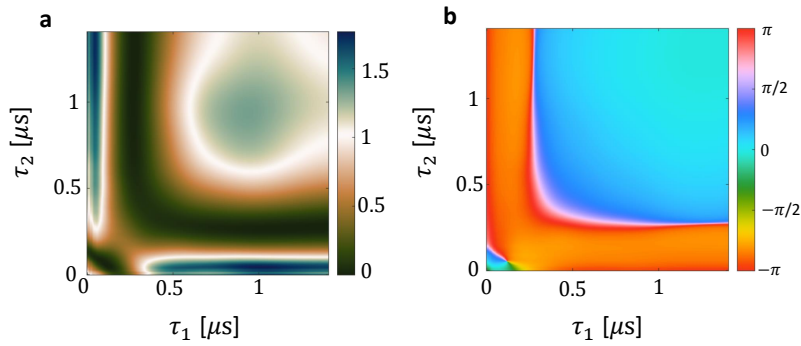


FIG. S1. Full numerical simulation of the three-photon normalized correlation function (a)  $g^{(3)}(\tau_1, \tau_2)$  (b)  $\phi^{(3)}(\tau_1, \tau_2)$  as a function of time separation between subsequent detections  $\tau_1 = t_2 - t_1$ ,  $\tau_2 = t_3 - t_2$ . Here, the OD=70 and other parameters are the same as given in Methods.

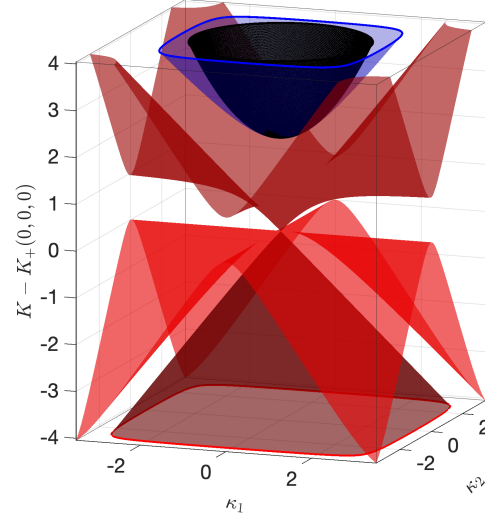


FIG. S2. **Analytical multiband model for  $N = 4$  photons.** The surfaces show momentum-space dispersion calculated following Eq. (24) for  $\kappa_3 = 0$ . Shaded paraboloid shows the Schrödinger approximation result, Eq. (25). The offset is  $K_+(0, 0, 0)/\sqrt{4} = \Omega^2/(c\Delta)$ , and all units are  $\omega_D$ .